

BAF-Detector: An Efficient CNN-Based Detector for Photovoltaic Solar Cell Defect Detection

Binyi Su, Haiyong Chen, and Zhong Zhou, *Member, IEEE*

Abstract—The multi-scale defect detection for solar cell electroluminescence (EL) images is a challenging task, due to the feature vanishing as network deepens. To address this problem, a novel Bidirectional Attention Feature Pyramid Network (BAFPN) is designed by combining the novel multi-head cosine non-local attention module with top-down and bottom-up feature pyramid networks through bidirectional cross-scale connections, which can make all layers of the pyramid share similar semantic features. In multi-head cosine non-local attention module, cosine function is applied to compute the similarity matrix of the input features. Furthermore, a novel object detector is proposed, called BAF-Detector, which embeds BAFPN into Region Proposal Network (RPN) in Faster RCNN+FPN to improve the detection effect of multi-scale defects in solar cell EL images. Finally, some experimental results on a large-scale EL dataset including 3629 images, 2129 of which are defective, show that the proposed method performs much better than other methods in terms of multi-scale defects classification and detection results in raw solar cell EL images.

Index Terms—photovoltaic solar cell, multi-scale defect detection, deep learning, cosine non-local attention, feature pyramid network

I. INTRODUCTION

THE multicrystalline solar cell defects will lead to a seriously negative impact on the power generation efficiency. Moreover, these defective cells will generate a lot of heat in the process of power generation, which may lead to fire and property loss [1]. Therefore, automated defect detection plays a vital role in the production process of solar cells, which can advantage safe and high-efficiency operation of the large-scale PV farms.

Solar cell defect detection aims to predict the class and location of multi-scale defects in a electroluminescence (EL) near-infrared image [2], [3], which is captured and processed by the following defect detection system. As is shown in Fig. 1, this intelligent system contains four components: supply subsystem, image acquisition subsystem, image process subsystem, and sort subsystem. By the image acquisition subsystem, the internal defects of solar cells that cannot be directly seen by the naked eye are clearly presented to us, as shown in Fig. 2. Regions of crystal silicon with higher conversion efficiency exhibit brighter luminescence in the sensed image.

This work was supported by National Key R&D Program of China under Grant 2018YFB2100601, National Natural Science Foundation of China under Grant 61872023, and National Natural Science Foundation of China under Grant 62073117. (*Corresponding author: Zhong Zhou.*)

B. Su, Z. Zhou are with the State Key Laboratory of Virtual Reality Technology and Systems, Beihang University, Beijing 100191, China (e-mail: Subinyi@buaa.edu.cn; zz@buaa.edu.cn).

H. Chen is with the School of Artificial Intelligence and Data Science, Hebei University of Technology, Tianjin 300130, China (e-mail: haiyong.chen@hebut.edu.cn).

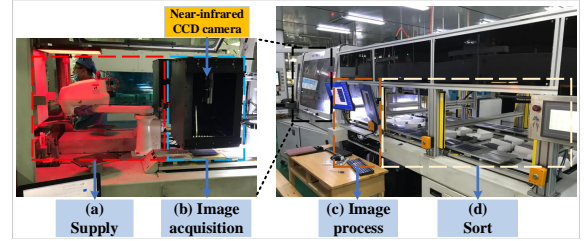


Fig. 1. Photovoltaic solar cell defect detection system.

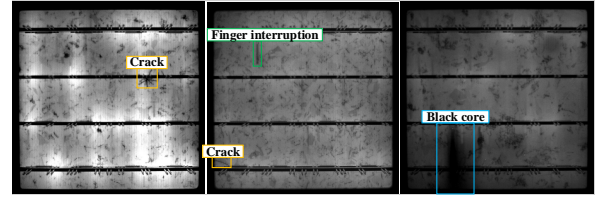


Fig. 2. Three raw EL near-infrared images with two crack defects in yellow boxes, one finger interruption defect in green box, one black core defect in blue box.

However, defects appear as dark regions because they are inactive and cannot emit light. Fig. 2 presents three raw EL near-infrared images with three types of defects: crack, finger interruption and black core under complex background disturbance. The shapes of crack defect mainly include line-like and star-like, which show random texture distribution and multi-scale characteristic. The finger interruption defect presents line-like shape and vertical distribution. Black core defect presents blob-like shape and is a cluster of black region in EL image. Except for the defects, the dislocation and four busbars also present as dark regions and may overlap with the defects sometimes. It causes automatic defect detection in solar cell EL images extremely difficult.

To automatically identify these defects in EL image, many conventional computer vision-based methods [4], [5] have been proposed to satisfy the urgent demand of the quality monitoring. Handcrafted features and data-based classifiers [6], [7] are usually the main tools, which use feature descriptors to generate the feature vectors of texture, color, shape, and spectral cues, and then, adopt classifiers to realize defects inspection. Feature extraction in conventional methods mainly relies on manually designed descriptors, which requires professional knowledge and a complicated parameter adjustment process. Moreover, each method targets to a specific application and has poor generalization ability and robustness.

Recently, deep learning models, particularly the convolutional neural network (CNN), have received substantial interest in industrial applications [8]–[15]. Deep learning is a data-

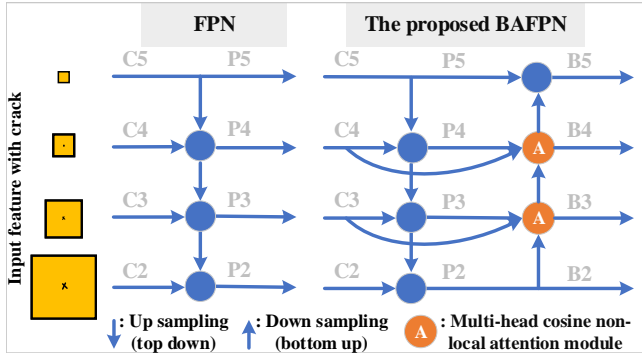


Fig. 3. The architecture of Feature Pyramid Network and the proposed Bidirectional Attention Feature Pyramid Network (BAFPN).

driven process. It presents the advantages of high accuracy, wide versatility, and strong plasticity. According to the learning of a large number of samples, the specific feature representation of the dataset can be obtained. The deep learning models are more robust and have more generalization ability. However, with the deepening and downsampling of the network during the training process, the features of small defects such as micro-crack, finger interruption are very easy to vanish. Poor feature representation will lead to poor detection result. Thus, how to retain the features of these small defects for prediction in the process of network deepening is crucial to improve the effectiveness of multi-scale solar cell defect detection task under complex background inference. Feature Pyramid Network [16] has the potential to solve this challenging problem. As shown in Fig. 3, the shallow layers contains much more small defect features than the deep layer, FPN integrates pyramid features of different scales from top to bottom, which is very beneficial for small defect detection. Subsequently, bottom-up path augmentation (PA-Net) [17], [18] is proposed to enhance the entire feature hierarchy with accurate localization signals in lower layers. This method shortens the information path between lower layers and topmost feature.

Inspired by above excellent works [16]–[18], Bidirectional Attention Feature Pyramid Network (BAFPN) is proposed in this paper, which is a multi-scale network that can be applied to pyramidal feature fusion. Different from above two feature fusion modules (FPN and PA-Net), BAFPN innovatively employs a novel multi-head cosine non-local attention module to capture the refined information of different scales from original feature and fused feature, which is beneficial to the bottom-up feature transfer. Moreover, the residual connection from the original feature to the multi-head cosine non-local attention module can guarantee the fully exploit of the same scale features. Finally, a BAF-Detector is proposed, which embeds BAFPN into Region Proposal Network (RPN) in Faster RCNN+FPN [16] to improve the detection effect of multi-scale defects in solar cell EL images. The main contributions of this paper are as follows.

- 1) A multi-head cosine non-local attention module is proposed by employing cosine function to calculate the feature similarity, which can achieve the highlighting of defect features and the suppression of background features simultaneously.
- 2) An Bidirectional Attention Feature Pyramid Network (BAFPN) is proposed to boost the bottom-up feature transfer, which is formed by combining multi-head cosine

non-local attention module with top-down and bottom-up feature pyramid networks through bidirectional cross-scale connections. BAFPN can make each scale layer have rich semantic features, which are beneficial to multi-scale defect detection.

- 3) An object detector, called BAF-Detector, is proposed, which embeds BAFPN into Region Proposal Network (RPN) in Faster RCNN+FPN. BAF-Detector has significantly improved the detection effect of multi-scale defects in EL images, which can meet the high-quality requirements of solar cell industrial production.

This paper is organized as follows: Section II presents an overview of the related works. Section III gives the details of the proposed methods. Section IV presents extensive experiments and ablation studies. Finally, Section V concludes this article.

II. RELATED WORKS

A. Automatic Defect Detection Methods

Hand-crafted feature based algorithm usually extract the image features such as color, texture, shape, and spatial relationship to train and test the discriminant classifiers for defect recognition. Demant *et al.* [4] introduced a pattern recognition approach based on local descriptors and support vector machines (SVM) classification, which improved the detection accuracy of the micro-crack defects in photoluminescence (PL) and EL images simultaneously. Su *et al.* [5] proposed a novel descriptor to extract the defect gradient feature in EL image, and adopted bag of feature strategy to capture the global information by similarity analysis and clustering. This method achieved promising results on solar cell patch dataset. Despite these methods achieving promising performance in specific situations, most are heavily rely on the expertise and cannot transfer directly between different applications.

At present, convolutional neural network (CNN) has become one of the most popular research direction in the field of computer vision [8]–[11], [13], [15]. CNN model has achieved a great success in image classification [8], [11], detection [15], [19], [20], segmentation [21], [22] and reconstruction [23] tasks. Thus, applying CNN to detect solar cell defect in EL image is of good prospect. Akram *et al.* [24] presented a novel approach using light CNN architecture for recognizing defects in EL images, which required less computational power and time. Chen *et al.* [25] proposed a weakly supervised CNN model with attention mechanism to accomplish surface defect classification and segmentation in solar cell image. Du *et al.* [26] introduced an CNN-based algorithm for efficient and innovative defect detection in existing industrial production line. This approach achieved successful application in Si-PV cell defects classification and detection task. Han *et al.* [13] proposed a defect segmentation method for polycrystalline silicon wafer based on deep learning. This method applied Region Proposal Network (RPN) to generate the underlying defect boxes, then a segmentation network was employed for pixel-wise defect region division. To suppress the complex background disturbance, Su *et al.* [15] proposed a novel Complementary Attention Network (CAN), which can adaptively compute the weights of the channel-wise or spatial attention map that will reweight and multiply with the CNN-extracted feature maps to achieve the suppression of noise interference features and the highlighting of object features. This proposed

method performs much better than other methods in terms of defects classification and detection in raw solar cell EL images. However, the detection effect of this method for multi-scale defects is not satisfactory, especially for micro-crack, which motivates this study.

B. CNN-based Detectors

The CNN detectors aim to classify and locate each object in the image with a suitable bounding box, which are mainly divided into two classes: (1) One is regression-based methods, (e.g., Retinanet [27], YOLOv3 [28]); (2) Another is region-based methods, (e.g., Faster RCNN [29], Mask RCNN [30]). The representative regression-based method is YOLOv3, which directly divides an image into small grids to predict bounding boxes by regression. Regression-based methods are very fast in object detection task at the expense of detection accuracy. Different from regression-based methods, region-based methods firstly generate many proposals that contains defects, then these proposals will be sent to the following network for class division and location predict. Region-based methods are superior in precision but require slightly more computation. Solar cell defect detection requires high detection accuracy to prevent defective cells from entering the next manufacturing process. Thus, to achieve a high-accuracy performance of defect detection in solar cell EL image, a region-based method is proposed to identify the fault cells in this paper.

C. Attention Mechanism

Attention model adaptively computes the weights of the channel-wise or spatial attention map that will reweight and multiply with the CNN-extracted feature maps to achieve the suppression of noise interference features and the highlighting of object features, which has been widely applied to various tasks [15], [31]–[34]. Wang *et al.* [31] proposed a non-local attention model to capture the contextual information of the object, which can boost feature representation ability of the image segmentation task. Shen *et al.* [32] employed channel-wise attention model to suppress the noise features of background and guide multi-scale feature fusion in object detection task. Zhou *et al.* [33] applied visual attention model and wavelet transform to detect defects in glass bottle bottom. Tang *et al.* [34] presented a new spatial attention bilinear CNN to detect defect in X-ray images of castings. Su *et al.* [15] proposed a novel Complementary Attention Network (CAN), which not only can suppress noise features of background, but also focuses on spatial locations of the defects in the solar cell EL images. In this paper, compared with the traditional non-local attention module, the multi-head cosine non-local attention module can better achieve the highlighting of defect features and the suppression of background features through cosine similarity calculation.

III. METHODOLOGY

In this section, we firstly introduce the proposed multi-head cosine non-local attention module, and then the architecture of the proposed BAF-Detector including BAFPN block is presented in details.

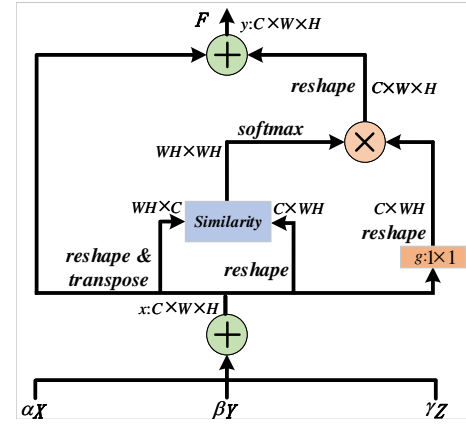


Fig. 4. Architecture of the proposed multi-head cosine non-local attention module. \oplus donates the element-wise addition, \otimes donates the matrix multiplication.

A. The Proposed Multi-head Cosine Non-Local Attention Module

The flowchart of multi-head cosine non-local attention module is illustrated in Fig. 4. Discriminant feature representations for defect and background in EL image are essential to fault identification, which can be accomplished by employing the attention module to highlight the defect feature and suppress the complicated background feature simultaneously. As for multi-head cosine non-local attention module, it depends on the normalized feature similarity matrix multiplying with the original input features to realize useful feature emphasize and disturbed feature suppression.

As illustrated in Fig. 4, the multi-head cosine non-local attention module represents that three feature spaces $X \in \mathbb{R}^{C \times W \times H}$, $Y \in \mathbb{R}^{C \times W \times H}$, and $Z \in \mathbb{R}^{C \times W \times H}$ are input into the attention module (C , W , and H are the channel number, width and height of the input feature maps respectively). α , β , and γ are the balance factors that are employed to reweight with each head respectively, which are all equal to 0.5 in this paper. The fused input feature x is defined as:

$$x = \alpha X + \beta Y + \gamma Z \quad (1)$$

The feature $x \in \mathbb{R}^{C \times W \times H}$ will be reshaped to $\mathbb{R}^{C \times N}$, where $N = WH$ represents the total position number in previous feature map. After that, the transposition of x will multiply with itself to calculate the cosine similarity map f . The similarity computing in original non-local attention module [31] is defined as:

$$f(x_i, x_j) = x_i^T x_j \quad (2)$$

where i and j are the index of a position in the input feature map $x \in \mathbb{R}^{C \times W \times H}$. Here $x_i^T x_j$ is dot-product similarity, which will be normalized by the following *softmax* operation to form the attention map.

$$s_{j,i} = \frac{\exp(f(x_i, x_j))}{\sum_{i=1}^N \exp(f(x_i, x_j))} \quad (3)$$

where $s_{j,i}$ measures the impact of i^{th} position on j^{th} position. There is a question for the dot-product similarity computing of non-local attention module, once most of numerator $\exp(f(x_i, x_j))$ are big values, the denominator

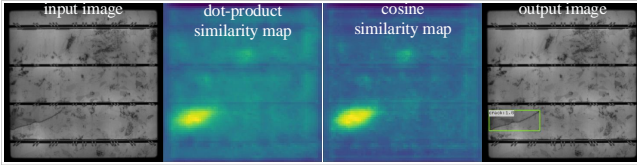


Fig. 5. Visualization of dot-product similarity map and cosine similarity map in B3 layer of the proposed BAF-Detector.

$\sum_{i=1}^N \exp(f(x_i, x_j))$ will be very large compared with numerator. Then, $s_{j,i}$ is close to zero, the difference between each element in s is very small. Thus, $s_{j,i}$ cannot be used to re-weight with the feature $g(x)$, where $g(x)$ is the output of a 1×1 convolution operation. To solve this problem, dot-similarity is replaced by the cosine similarity, which will limit all elements $f(x_i, x_j)$ to $[-1, 1]$. After being normalized by *softmax*, these elements are suitable to keep their differences. The cosine similarity matrix is defined as:

$$f(x_i, x_j) = \frac{x_i^T x_j}{\|x_i\| \|x_j\|} \quad (4)$$

where $\|x_i\|$ and $\|x_j\|$ are the norms of vectors x_i and x_j respectively. Noting that cosine similarity can make non-local attention acquire more discriminant features, which achieves better performance than dot-similarity to highlight the useful feature and suppress the complex background feature, as shown in Fig. 5. It is not difficult to see that the cosine similarity map is better than the dot-product similarity map, whether the emphasize of defect feature or the suppression of complex background.

Refer to Eq. 3, the *softmax* function is employed to normalize the similarity map to form the attention map, which will multiply with the reshaped feature $g(x) \in \mathbb{R}^{C \times N}$. Finally, the result will be reshaped to $\mathbb{R}^{C \times W \times H}$, and perform a element-wise sum operation with the input features x . The output $y \in \mathbb{R}^{C \times W \times H}$ of the multi-head cosine non-local attention module is defined as:

$$y_j = \sum_{i=1}^N s_{j,i} g(x_i) + x_i \quad (5)$$

It can be inferred from Eq. 5 that the resulting feature y at each position is a weighted sum of the features across all positions and original features. The similar semantic features achieve mutual benefits, improving intra-class compact and semantic consistency, which presents highlighting region in the similarity map. Code are available at <https://github.com/binyisu/cosine-nonlocal>.

B. Defect detection

In this paper, we use Faster RCNN+FPN [16] as the base detector to detect multi-scale defects in EL near-infrared images such as crack, finger interruption, and black core, while integrating a novel Bidirectional Attention Feature Pyramid Network (BAFPN) into RPN. We firstly introduce the proposed BAFPN block, then illustrate the details of proposed defect detection architecture BAF-Detector.

1) *Bidirectional Attention Feature Pyramid Network (BAFPN)*: To obtain more refined fusion features of pyramidal layers, a novel Bidirectional Attention Feature Pyramid Network (BAFPN) is designed by combining the novel multi-head cosine non-local attention module with top-down and bottom-up feature pyramid networks through bidirectional cross-scale connections, which can accomplish informative feature aggregation of multi-scale layers. In BAFPN, multi-head cosine non-local attention module plays a key role in feature refinement.

As shown in Fig. 6, multi-scale features are aggregated by the BAFPN block at different resolutions. Formally, given a list of multi-scale features (C2, C3, C4, C5), the goal of BAFPN block is to find a transform function that can effectively aggregate different features and output a list of new refined features. The top-down and bottom-up feature fusion process is defined as:

$$P5 = \text{conv}(C5), P4 = \text{up}(P5) + \text{conv}(C4), \quad (6)$$

$$P3 = \text{up}(P4) + \text{conv}(C3), P2 = \text{up}(P3) + \text{conv}(C2)$$

$$B2 = \text{conv}(P2),$$

$$B3 = A(\text{conv}(C3), \text{conv}(P3), \text{down}(B2)), \quad (7)$$

$$B4 = A(\text{conv}(C4), \text{conv}(P4), \text{down}(B3)),$$

$$B5 = \text{conv}(P5) + \text{down}(B4), B6 = \text{max pool}(B5)$$

where *up* represents upsampling, *down* represents down-sampling, *max pool* represents max pooling and *conv* is a convolutional operation for feature filtering. $A(\cdot)$ is the operation of proposed multi-head cosine non-local attention module. Rich textural features in lower layers by bottom-up path augmentation shorten the information path between lower layers and topmost feature [17]. Moreover, the outputs of two middle layers ($B3$ and $B4$) are refined by attention mechanism, which will highlight the defect feature and suppress the complex background feature during the solar cell EL image defect detection task. The reason why attention modules are only used in the middle two layers of BAFPN is that on the one hand the multi-head cosine non-local attention module has a heavy computational burden. If it is used in every layer of FPN, it will cause our sever out of memory. On the other hand, the middle two layers of FPN are a compromise between useful semantic features and texture features, then using the attention module to refine the features of these two layers will maximize the benefits.

By above computation, the outputs are the features after fusion of different scales. The pyramidal features fusion can increase the robustness to scale variance, all layers of our pyramid share similar semantic features.

2) *Overview of Defect Detection Architecture*: As illustrated in Fig. 6, the flowchart of the proposed BAF-Detector is divided into three parts: feature extraction, region proposal (BAFPN-RPN), classification and detection. Firstly, ImageNet-pretrained ResNet101 [35] is employed as the backbone network to extract the features of the EL image. Secondly, the extracted features of different layers will be transmitted to the proposed BAFPN-RPN module, which will generate many region proposals that may contain a defect. Thirdly, the features for each proposal are generated by corresponding to the multi-level features of ResNet101, next the Region of Interest (RoI) pooling layer will pool the produced features

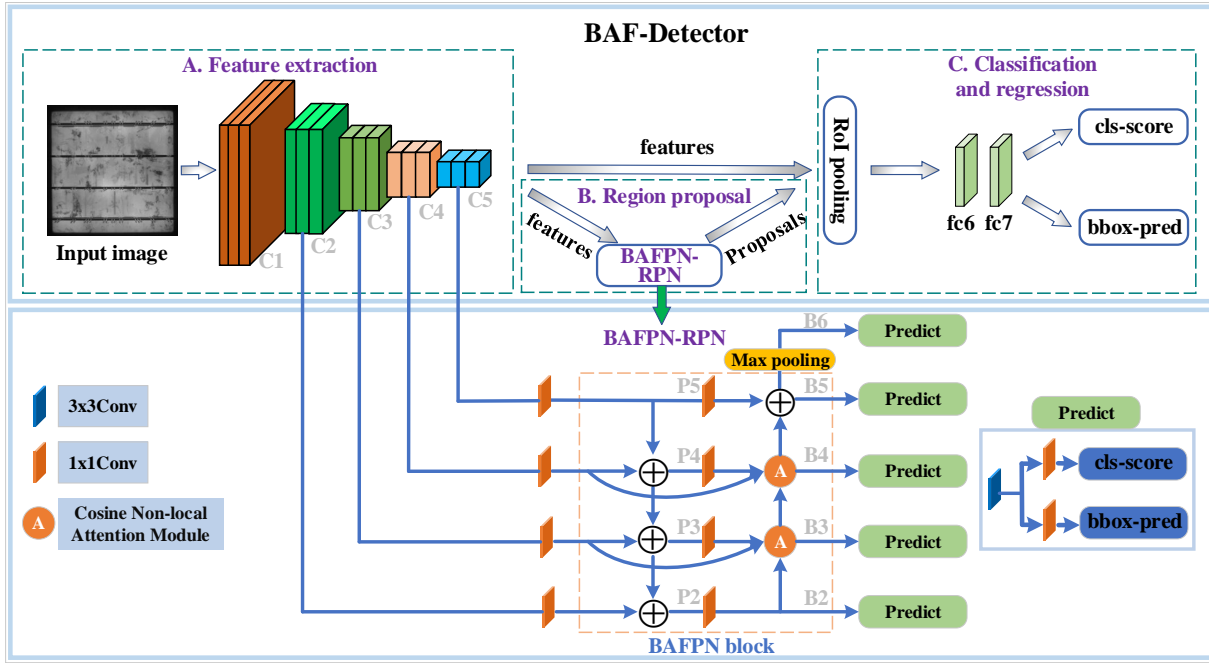


Fig. 6. The architecture of the proposed Bidirectional Attention Feature Pyramid Network Detector (BAF-Detector).

into a fixed-length feature vector. After that, two hidden 1024-d fully connected layers is attached before two output layers: one outputs classification scores over K object classes plus a “background” class and the other outputs refined bounding-box positions for each of the K object classes. As the first stage of BAF-Detector architecture, each predicted head of BAFPN-RPN can be trained by optimizing the following loss function:

$$L(\{p_i\}, \{t_i\}) = \frac{1}{N_{cls}} \sum_i L_{cls}(p_i, p_i^*) + \lambda \frac{1}{N_{reg}} \sum_i p_i^* L_{reg}(t_i, t_i^*) \quad (8)$$

where i is the index of an anchor box [29] in a mini-batch and p_i is the predicted probability of anchor box i containing a defect. If the anchor box is predicted to contain a defect, the ground-truth label p_i^* is 1, otherwise p_i^* is 0. t_i is a vector representing the 4 parameterized coordinates of the predicted bounding box, and t_i is that of the ground-truth box associated with a defective anchor box. The term $p_i^* L_{reg}$ means the regression loss is activated only for defective anchor ($p_i = 1$) and is disabled otherwise ($p_i = 0$). The outputs of the `cls_score` layer and `bbox_pred` layer consist of p_i and t_i respectively. The classification loss L_{cls} is log loss over two classes (defect or not defect). For the regression loss, we use $L_{reg}(t_i, t_i^*) = R(t_i - t_i^*)$ where R is the robust loss function (smooth L1) defined as follows:

$$smooth_{L1}(x) = \begin{cases} 0.5x^2 & \text{if } |x| < 1 \\ |x| - 0.5 & \text{otherwise} \end{cases} \quad (9)$$

The term $p_i^* L_{reg}$ means the regression loss is activated only for defective anchor boxes ($p_i = 1$) and is disabled otherwise ($p_i = 0$). Referring to Faster RCNN+FPN, the two terms are normalized by $N_{cls} = 256$ and $N_{reg} = 2400$, and weighted

by a balancing parameter $\lambda = 10$, thus both cls and reg terms are roughly equally weighted.

For bounding box regression, the parameterizations of the 4 coordinates is defined as follows:

$$t_x = \frac{x - x_a}{w_a}, \quad t_y = \frac{y - y_a}{h_a} \quad (10)$$

$$t_w = \log\left(\frac{w}{w_a}\right), \quad t_h = \log\left(\frac{h}{h_a}\right) \quad (11)$$

$$t_x^* = \frac{x^* - x_a}{w_a^*}, \quad t_y^* = \frac{y^* - y_a}{h_a^*} \quad (12)$$

$$t_w^* = \log\left(\frac{w^*}{w_a^*}\right), \quad t_h^* = \log\left(\frac{h^*}{h_a^*}\right) \quad (13)$$

where x , y , w and h donate the center coordinates, width and height of the box. Variables x , x_a , and x^* are for the predicted box, anchor box and ground-truth box, respectively (y , w , h are same as this). Otherwise, this can be thought of as bounding-box regression from an anchor box to a nearby ground-truth box.

IV. EXPERIMENTAL RESULTS

In this section, experimental steps such as dataset construction, evaluation matrix, implementation details, quantitative experimental evaluation, time efficiency evaluation, and ablation studies are presented. To understand and show the improvement directly, the visualization of similarity map is used as a powerful tool to support experimental results.

A. Dataset

We evaluate the experimental results of our proposed BAF-Detector on our solar cell EL image dataset. In this dataset, 2129 EL defective images and 1500 good images with raw resolution of 1024×1024 are used to evaluate the classification and detection effectiveness of our proposed BAF-Detector. Table I shows the raw dataset distribution of training data and testing data. For the ground truth of different defects (crack,

finger interruption, and black core), we use a python dataset annotation library (LabelImg) to make the EL image dataset referring to VOC2007 format, which just needs a box to tightly contain the defect and do not need too much expert experience. The standard VOC2007 format EL image dataset can ensure the fairness comparison between different detectors. This dataset include three files: 1) Annotations; 2) ImageSets; 3) JPEGImages. The Annotations file is mainly composed of xml file, which includes defect ground truth information. The ImageSets file includes a Main file, in which four text files (train.txt, test.txt, trainval.txt, and val.txt) divide the dataset. The original EL images are placed in the JPEGImage file. The proposed BAF-Detector and these detectors used for comparison can be directly trained and tested in the standard VOC2007 EL image dataset.

B. Evaluation metrics

We evaluate the performance of defect classification by the following evaluation metrics such as Precision (P), Recall (R) and F-measure (F). Moreover, Average Precision (AP), mean Average Precision (mAP) and Mean Intersection over Union (MIoU) are used to evaluate defect detection effect. Parameters number and frames per second (FPS) are the metrics used to asses the time efficiency. The aforesaid metrics are defined as

$$Precision = \frac{TP}{TP + FP} \times 100\% \quad (14)$$

$$Recall = \frac{TP}{TP + FN} \times 100\% \quad (15)$$

$$F - measure = \frac{2 \times Precision \times Recall}{Precision + Recall} \quad (16)$$

$$IoU = \frac{DetectionResult \cap GroundTruth}{DetectionResult \cup GroundTruth} \quad (17)$$

where TP and FN are the number of defect images, which are predicted to be correct or not; FP represents the number of non-defect, which is misclassified; $DetectionResult$ is the defect detected box of the detector; $GroundTruth$ is the real manual labeling box of the defect.

C. Implementation Details

The experiments are conducted on a work station with a Intel Core i7-10700 CPU and a NVIDIA GeForce RTX 2070 SUPER. The pre-trained model on Imagenet is used to initialize the ResNet101, which can accelerate convergence of the network. The learning-rate is set to 0.001. The class number is set to 3. The batch size is set to 1 and the max iteration is fixed to 40000, which can ensure the fully loop through of the solar cell EL training data. In BAFPN-RPN, the stride of *max pooling* is 2. Moreover, a scale level is assigned with an anchor, which has three aspect ratios [0.5, 1, 2] at each level. The anchors is defined to have areas of $\{32^2, 64^2, 128^2, 256^2, 512^2\}$ pixels on $\{B2, B3, B4, B5, B6\}$ respectively [16], and anchors with different scales are responsible for predicting defects of different sizes. In the experiments, all input EL images are extended to three channels and resized to 600×600 pixels. The detailed information and hyperparameters of the BAF-Detector are presented in Table II, which can help the readers to better understand our method.

TABLE I
DISTRIBUTION OF SOLAR CELL EL DATASET. CK, FR, BC: THE EL IMAGE CONTAINS ONLY ONE TYPE OF DEFECT: CRACK, FINGER INTERRUPTION OR BLACK CORE. CK&FR: THE EL IMAGE CONTAINS TWO TYPES OF DEFECTS: CRACK AND FINGER INTERRUPTION.

Dataset (EL images)	Defective images				Good images	Total
	Ck	Fr	Ck&Fr	Bc		
Training	260	252	85	250	/	847
Testing	393	521	97	271	1500	2782
Total	2129				1500	3629

TABLE II
HYPERPARAMETERS OF BAF-DETECTOR

	DECAY_STEP	DECAY_FACTOR	WEIGHT_DECAY	MOMENTUM
Training	15000, 30000	10	0.0001	0.9
	IMG_SHORT_SIDE_LEN	IMG_MAX_LENGTH	BASE_ANCHOR_SIZE_LIST	BATCH_SIZE
	600	1000	[32, 64, 128, 256, 512]	1
Testing	classification score threshold		non-maximum suppression threshold	
	0.3		0.5	

D. Evaluation

The proposed BAF-Detector is compared with YOLOv3, Faster RCNN, and Faster RPN-CNN in the classification and detection performance on the solar cell EL image dataset, which are presents in Table III.

1) *Classification Evaluation*: In terms of the defective images classification results, the proposed BAF-Detector achieves a better performance than other detectors on each quantitative evaluation metric, such as precision (99.21%), recall (98.20%) and F-measure (98.70%). The high recall rate of the proposed BAF-Detector ensures that the defective solar cell is not easy to be missed during the intelligent manufacturing process, which is essential to the high-quality production of solar cells.

2) *Detection Evaluation*: In terms of the proposed model in defect detection performance, mAP and MIoU are employed to evaluate the quantitative comparisons. Table III shows the detection results of one-stage detector (YOLOv3) and two-stage detectors (the others) with same training and testing EL image dataset. With embedding the proposed BAFPN block into RPN in Faster RCNN+FPN, the BAF-Detector outperforms other detectors in the defect detection effects.

The P/R curves of different defects using our proposed BAF-Detector are shown in Fig. 7. The detection result of the black core defect is the best, the AP value reaches 100%. Black core defect has a single blob-like shape and a large scale, which causes it easy to be detected. The detection result of finger interruption defect is also easier to be detected, due to the vertical strip distribution. The detection result of crack defect is the worst, because of the random shapes and different scales especially for micro-crack, which bring some challenges to detect it in solar cell EL images.

Fig. 8 shows some intermediate and final detection results. As can be seen, the similarity maps of low layer B3 or deep layer B4 in BAFPN retain the informative features of multi-scale defects during the network deepens. Moreover, the noise background features are suppressed simultaneously. Thus, we can conclude that the BAFPN boosts the bottom-up feature transfer as the network deepens. It enables the BAF-Detector to better detect multi-scale defects in EL images.

TABLE III
THE EXPERIMENTAL RESULTS OF DIFFERENT DETECTORS ON OUR SOLAR CELL EL IMAGE DATASET.

Detectors	Classification			Detection		Parameters	FPS
	P(%)	R(%)	F(%)	mAP(%)	MIoU(%)		
YOLOv3 [15]	86.73	97.3	91.71	78.79	64.96	58.73M	11.36
Faster RCNN [15]	93.53	96.04	94.77	83.11	68.22	360.50M	6.41
Faster RPN-CNN [15]	99.17	97.78	98.47	87.38	71.42	261.26M	5.95
Our BAF-Detector	99.21	98.2	98.70	88.07	73.29	120.87M	7.75

TABLE IV
THE ABLATION STUDIES OF THE PROPOSED BAF-DETECTOR ON OUR SOLAR CELL EL IMAGE DATASET WITH DIFFERENT COMPONENTS. \oplus : ADDITION OPERATION IS USED TO REPLACE THE ATTENTION MODULE. MT: MIDDLE TWO SCALE LEVELS, ATTENTION MODULES ARE USED IN THE MIDDLE TWO LEVELS OF FPN.

FPN	Attention	Classification			Detection		Parameters	FPS
		P(%)	R(%)	F(%)	mAP(%)	MIoU(%)		
top-down	$\times(\oplus)$	94.62	96.72	95.66	85.21	70.53	115.11M	7.81
top-down	$\checkmark(\text{dot-product,mt})$	95.87	97.42	96.64	86.97	71.54	115.37M	7.78
top-down	$\checkmark(\text{cosine,mt})$	96.18	97.86	97.01	87.14	72.56	115.37M	7.79
top-down+bottom-up	$\times(\oplus)$	95.13	97.07	96.09	85.67	72.32	119.87M	7.75
top-down+bottom-up	$\checkmark(\text{dot-product,mt})$	98.58	97.91	98.24	87.69	72.58	120.87M	7.69
top-down+bottom-up	$\checkmark(\text{cosine,mt})$	99.21	98.20	98.70	88.07	73.29	120.87M	7.68

3) *Overall Evaluation*: From above classification and detection evaluation of the proposed BAF-Detector, we can conclude that the proposed BAF-Detector outperforms other detectors in the EL image defect classification and detection performance. The reason is that the fusion strategy (BAFPN) can employ the proposed multi-head cosine non-local attention module and the top-down bottom-up FPN to highlight target feature, suppress complex background feature, and better guide pyramidal feature fusion, which is very beneficial for multi-scale defect classification and detection tasks under complex background interference in solar cell EL image dataset.

4) *Time-efficiency Evaluation*: The results of FPS is the average of 1287 testing defective EL image, which is conducted on a work station with a GPU. As we can see from Table III, the FPS of a detector is inversely proportional to the parameter number. Our BAF-Detector achieves 7.75 frame per second (FPS). Although our method is not the fastest, but it outperforms other detectors in defect inspection accuracy that is essential to the industrial production.

E. Ablation Studies

1) *Effect of Attention Module*: To confirm the effectiveness of the proposed multi-head cosine non-local attention module, the strategy of add or replace the attention module is employed for ablation studies. As illustrated in Table IV, by comparing two similarity calculation methods of non-local (dot-product) and cosine non-local (cosine), it can be demonstrated that cosine similarity outperforms dot-product similarity in the solar cell defect inspection task. The visualization of similarity maps are shown in Fig. 5. For the second row of the comparisons, defect regions can be highlighted more clearly by cosine similarity map, and the background is more fully suppressed. Moreover, the performance of adding attention module is better than removing it.

2) *Effect of Bidirectional Attention Feature Pyramid Network (BAFPN)*: The effect of the top-down bottom-up FPN with attention module (BAFPN) can be seen in the last two rows in Table IV. By comparing the proposed BAFPN with other structures, we find that BAFPN achieves a better performance than the experimental results of the first four rows, which illustrates that the BAFPN block outperforms others

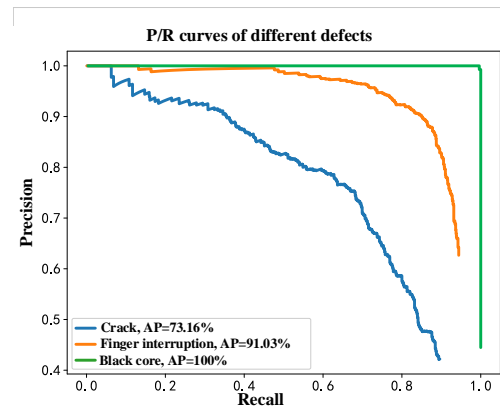


Fig. 7. The P/R curves of the three types of defects.

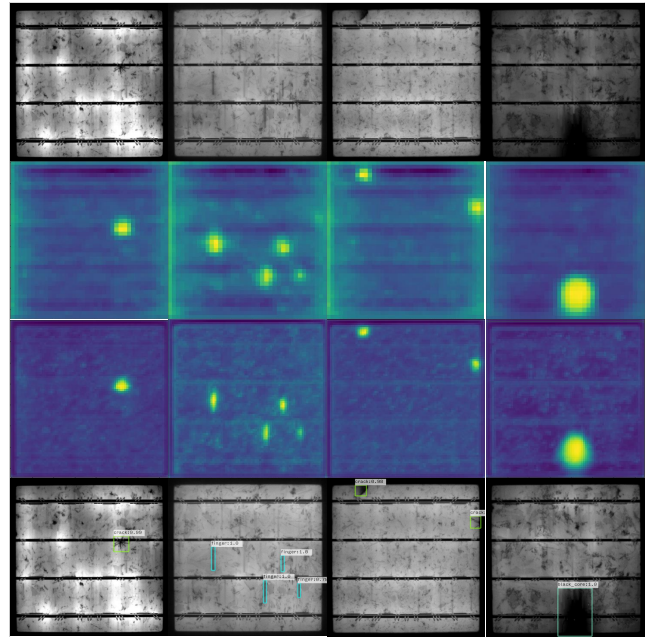


Fig. 8. Visualization of intermediate and final detection results. The first row is the input, the second row is the similarity map of B4 layer, the third row is the similarity map of B3 layer, and the fourth row is the output.

in terms of multi-scale defect detection. However, BAFPN has 4.77% more parameters than original FPN, which slightly increases computational burdens.

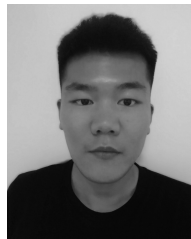
V. CONCLUSION

In this paper, a novel Cosine Non-local Attention module is proposed to highlight the defect feature and suppress the complex background feature. The novel attention module is also used to construct an efficient multi-scale feature fusion block BAFPN, which combines with RPN in Faster RCNN+FPN to form a defect detection model BAF-Detector. The multi-scale defects in solar cell EL image are effectively detected under the disturbance of the complex background. The proposed BAF-Detector outperforms other detectors in each quantitative metric, which demonstrates that our proposed deep learning model has certain advantages in defect inspection, and provides a practical solution for research and applications of solar cell defect detection.

There are also some limitations for our BAF-Detector. For example, the feature balance factors α , β and γ in attention module are set mutually, which takes time and efforts. In the future, adaptive methods will be researched to automatically determine these factors.

REFERENCES

- [1] A. H. Herraiz, A. P. Marugan, and F. P. G. Marquez, "Photovoltaic plant condition monitoring using thermal images analysis by convolutional neural network-based structure," *Renew. Energ.*, vol. 153, no. 1, pp. 334–348, Feb. 2020.
- [2] T. Fuyuki and A. Kitiyanan, "Photographic diagnosis of crystalline silicon solar cells utilizing electroluminescence," *Appl. Phys. A. Solids Surf.*, vol. 96, no. 1, pp. 189–196, Jul. 2009.
- [3] M. Dhimish and V. Holmes, "Solar cells micro-crack detection technique using state-of-the-art electroluminescence imaging," *J. Sci-Adv. Mater. Dev.*, vol. 4, no. 4, pp. 499–508, Oct. 2019.
- [4] M. Demant *et al.*, "Microcracks in silicon wafers i: Inline detection and implications of crack morphology on wafer strength," *IEEE J. Photovolt.*, vol. 6, no. 1, pp. 126–135, Jan. 2016.
- [5] B. Su, H. Chen, Y. Zhu, W. Liu, and K. Liu, "Classification of manufacturing defects in multicrystalline solar cells with novel feature descriptor," *IEEE Trans. Instrum. Meas.*, vol. 68, no. 12, pp. 4675–4688, Mar. 2019.
- [6] K. Firuzi, M. Vakilian, B. T. Phung, and T. R. Blackburn, "Partial discharges pattern recognition of transformer defect model by LBP HOG features," *IEEE Trans. Power. Deliver.*, vol. 34, no. 2, pp. 542–550, Apr. 2019.
- [7] Q. Luo *et al.*, "Generalized completed local binary patterns for time-efficient steel surface defect classification," *IEEE Trans. Instrum. Meas.*, vol. 68, no. 3, pp. 667–679, Mar. 2019.
- [8] F. C. Chen *et al.*, "NB-CNN: Deep learning-based crack detection using convolutional neural network and naive bayes data fusion," *IEEE Trans. Ind. Electron.*, vol. 65, no. 99, pp. 4392–4400, May. 2018.
- [9] C. Hu and Y. Wang, "An efficient convolutional neural network model based on object-level attention mechanism for casting defect detection on radiography images," *IEEE Trans. Ind. Electron.*, vol. 67, no. 12, pp. 10922–10930, Jan. 2020.
- [10] P. Sassi, P. Tripicchio, and C. A. Avizzano, "A smart monitoring system for automatic welding defect detection," *IEEE Trans. Ind. Electron.*, vol. 66, no. 12, pp. 9641–9650, Feb. 2019.
- [11] M. W. Akram, G. Li, Y. Jin, X. Chen, and A. Ahmad, "CNN based automatic detection of photovoltaic cell defects in electroluminescence images," *Energ.*, vol. 189, no. 10, pp. 1–15, Dec. 2019.
- [12] H. Chen, Y. Pang, Q. Hu, and K. Liu, "Solar cell surface defect inspection based on multispectral convolutional neural network," *J. Intell. Manuf.*, vol. 31, no. 2, pp. 453–468, Dec. 2020.
- [13] H. Han *et al.*, "Polycrystalline silicon wafer defect segmentation based on deep convolutional neural networks," *Pattern Recognit. Lett.*, vol. 130, no. 2, pp. 234–241, Feb. 2020.
- [14] X. Wei, S. Jiang, Y. Li, C. Li, L. Jia, and Y. Li, "Defect detection of pantograph slide based on deep learning and image processing technology," *IEEE Trans. Intell. Transp.*, vol. 21, no. 3, pp. 947–958, Mar. 2020.
- [15] B. Su *et al.*, "Deep learning-based solar-cell manufacturing defect detection with complementary attention network," *IEEE Trans. Ind. Inform.*, DOI 10.1109/TII.2020.3008021, 2020.
- [16] T. Lin, P. Dollar, R. Girshick, K. He, B. Hariharan, and S. Belongie, "Feature pyramid networks for object detection," in *Proc. IEEE Conf. Comput. Vis. Pattern Recognit.*, 2017, pp. 2117–2125.
- [17] S. Liu, L. Qi, H. Qin, J. Shi, and J. Jia, "Path aggregation network for instance segmentation," in *Proc. IEEE Conf. Comput. Vis. Pattern Recognit.*, 2018, pp. 8759–8768.
- [18] M. Tan and Q. V. Le, "Efficientnet: Rethinking model scaling for convolutional neural networks," 2020, [Online]. Available: <http://arxiv.org/abs/1905.11946>
- [19] X. Zhang *et al.*, "Detection of surface defects on solar cells by fusing multi-channel convolution neural networks," *Infrared Phys. Techn.*, vol. 108, no. 4, pp. 127–132, Apr. 2020.
- [20] J. Liu, C. Wang, H. Su, B. Du, and D. Tao, "Multistage GAN for fabric defect detection," *IEEE Trans. Image Process.*, vol. 29, no. 12, pp. 3388–3400, Dec. 2020.
- [21] T. Nakazawa and D. V. Kulkarni, "Anomaly detection and segmentation for wafer defect patterns using deep convolutional encoder-decoder neural network architectures in semiconductor manufacturing," *IEEE Trans. Semiconduct. M.*, vol. 32, no. 2, pp. 250–256, May. 2019.
- [22] J. Fu, J. Liu, H. Tian, Y. Li, Y. Bao, Z. Fang, and H. Lu, "Dual attention network for scene segmentation," in *Proc. IEEE Conf. Comput. Vis. Pattern Recognit.*, 2019, pp. 3141–3149.
- [23] B. Su, L. Yu and W. Yang, "Event-Based High Frame-Rate Video Reconstruction With A Novel Cycle-Event Network," in *Proc. IEEE Inter. Conf. Image Process.*, 2020, pp. 86–90,
- [24] M. Waqar Akram *et al.*, "Improved outdoor thermography and processing of infrared images for defect detection in pv modules," *Sol. Energy*, vol. 190, no. 9, pp. 549–560, Sep. 2019.
- [25] H. Chen, Q. Hu, B. Zhai, H. Chen, and K. Liu, "A robust weakly supervised learning of deep conv-nets for surface defect inspection," *Neural Comput. Appl.*, vol. 32, no. 15, pp. 11229–11244, Mar. 2020.
- [26] B. Du, Y. He, Y. He, J. Duan, and Y. Zhang, "Intelligent classification of silicon photovoltaic cell defects based on eddy current thermography and convolution neural network," *IEEE Trans. Ind. Inform.*, vol. 16, no. 10, pp. 6242–6251, Oct. 2020.
- [27] T. Lin, P. Goyal, R. Girshick, K. He, and P. Dollár, "Focal loss for dense object detection," *IEEE Trans. Pattern Anal.*, vol. 42, no. 2, pp. 318–327, Feb. 2020.
- [28] J. Redmon and A. Farhadi, "Yolov3: An incremental improvement," Apr. 2018. [Online]. Available: <https://arxiv.org/pdf/1804.02767>.
- [29] S. Ren, K. He, R. Girshick, and J. Sun, "Faster r-cnn: Towards real-time object detection with region proposal networks," *IEEE Trans. Pattern Anal.*, vol. 39, no. 6, pp. 1137–1149, Jun. 2017.
- [30] K. He, G. Gkioxari, P. Dollár, and R. B. Girshick, "Mask R-CNN," 2017, [Online]. Available: <http://arxiv.org/abs/1703.06870>
- [31] X. Wang, R. Girshick, A. Gupta, and K. He, "Non-local neural networks," 2018, [Online]. Available: <https://arxiv.org/abs/1711.07971>
- [32] Z. Shen *et al.*, "Improving object detection from scratch via gated feature reuse," 2019, [Online]. Available: <https://arxiv.org/abs/1712.00886>
- [33] C. Zhou, M. Wu, and S. K. Lam, "SSA-CNN: Semantic self-attention cnn for pedestrian detection," 2019, [Online]. Available: <https://arxiv.org/abs/1902.09080v1>
- [34] Z. Tang *et al.*, "Nondestructive defect detection in castings by using spatial attention bilinear convolutional neural network," *IEEE Trans. Ind. Inform.*, vol. 17, no. 1, pp. 82–89, Jan. 2021.
- [35] K. He *et al.*, "Deep residual learning for image recognition," in *Proc. IEEE Conf. Comput. Vis. Pattern Recognit.*, 2016, pp. 770–778.



Binyi Su received the B.S. degree in intelligent science and technology from the Hebei University of Technology, Tianjin, China, in 2017, and the M.S. degree in control engineering from the Hebei University of Technology, Tianjin, China, in 2020.

He is currently pursuing the Ph.D. degree in computer science and technology from Beihang University, Beijing, China. His current research interests include computer vision and pattern recognition, machine learning and artificial intelligence, industrial image defect detection.



Haiyong Chen received the M.S. degree in detection technology and automation from the Harbin University of Science and Technology, Harbin, China, in 2005, and the Ph.D. degree in control science and engineering from the Institute of Automation, Chinese Academy of Sciences, Beijing, China, in 2008.

He is currently a Professor with the School of Artificial Intelligence and Data Science, Hebei University of Technology, Tianjin. He is also an expert in the field of photovoltaic cell image processing and automated production equipment. His current research interests include image processing, robot vision, and pattern recognition.



Zhong Zhou (Member, IEEE) received the B.S. degree in material physics from Nanjing University in 1999 and the Ph.D. degree in computer science and technology from Beihang University, Beijing, China, in 2005.

He is currently a Professor and the Ph.D. Adviser with the State Key Laboratory of Virtual Reality Technology and Systems, Beihang University. His main research interests include virtual reality, augmented reality, mixed reality, computer vision, and artificial intelligence. He is

a member of ACM and CCF.